

An edited version of this paper was published by AGU.
Copyright (2008) American Geophysical Union.

Spreen, G., L. Kaleschke, and G. Heygster (2008), Sea ice remote sensing using AMSR-E 89-GHz channels, *J. Geophys. Res.*, **113**, C02S03, doi:10.1029/2005JC003384.

To view the published open abstract, go to <http://dx.doi.org> and enter the DOI.

Sea Ice Remote Sensing Using AMSR-E 89 GHz Channels

G. Spreen

Institute of Oceanography, University of Hamburg, Hamburg, Germany

L. Kaleschke

Institute of Environmental Physics, University of Bremen, Bremen, Germany
now at: Institute of Oceanography, University of Hamburg, Hamburg, Germany

G. Heygster

Institute of Environmental Physics, University of Bremen, Bremen, Germany

Abstract. Recent progress in sea ice concentration remote sensing by satellite microwave radiometers has been stimulated by two developments: First, the new sensor AMSR-E offers spatial resolutions of approximately 6x4 km at 89 GHz, nearly three times the resolution of the standard sensor SSM/I at 85 GHz (15x13 km). Second, a new algorithm enables to estimate sea ice concentration from the channels near 90 GHz, despite the enhanced atmospheric influence in these channels. This allows to fully exploit their horizontal resolution which is up to four times finer than the one of the channels near 19 and 37 GHz, the frequencies used by the most widespread algorithms for sea ice retrieval, the NASA-Team and Bootstrap algorithms. The ASI algorithm used combines a model for retrieving the sea ice concentration from SSM/I 85 GHz data proposed by *Svendsen et al.* [1987] with an ocean mask derived from the 18-, 23-, and 37-GHz AMSR-E data using weather filters. During two ship campaigns, the correlation of ASI, NASA-Team 2 and Bootstrap algorithms ice concentrations with bridge observations were 0.80, 0.79 and 0.81, respectively. Systematic differences over the complete AMSR-E period (2002-2006) between ASI and NASA-Team 2 are below $-2\pm 8.8\%$, and between ASI and Bootstrap $1.7\pm 10.8\%$. Among the geophysical implications of the ASI algorithm are: (1) Its higher spatial resolution allows to better estimate crucial variables in numerical atmospheric and ocean models, e.g. the heat flux between ocean and atmosphere, especially near coastlines and in polynyas. (2) It provides an additional time series of ice area and extent for climate studies.

1. Introduction

The important role of sea ice in the climate system is widely accepted [e.g. *Aagaard and Carmack*, 1989; *Liu et al.*, 2004; *Vavrus and Harrison*, 2003]. It covers a significant fraction (5% to 8% [*Comiso*, 2003]) of the ocean and has a high variability in time. Due to the high albedo of ice in comparison to water there is a positive heat balance feedback connected with the ice cover [*Wadhams*, 2000]. Moreover, sea ice reduces the heat transfer between ocean and atmosphere in the polar regions, and the production of sea ice is important for the deep water formation in the Greenland Sea and Weddell Sea. Additionally the distribution of sea ice impacts the operation of vessels and other sea based structures like oil platforms.

For these reasons it is necessary to obtain accurate and high resolution (in space and time) information about the distribution of sea ice. Sea ice concentration, i.e. the percentage of a given area covered with sea ice, has been retrieved by passive microwave sensors since the start of the ESMR (Electrically Scanning Microwave Radiometer) sensor in December 1972. Since 1987 the SSM/I (Special Sensor Microwave/Imager) has been widely used for sea ice concentration determination. A restriction of these instruments is the coarse spatial resolution of the data. Since 1992 the 85 GHz channels of SSM/I with a higher spatial resolution became available.

In 2002 two new microwave radiometers were launched. AMSR-E (Advanced Microwave Scanning Radiometer for EOS) in May on the AQUA platform and AMSR (Advanced Microwave Scanning Radiometer) in October on the MIDORI-II (formerly ADEOS-II) satellite. Control over MIDORI-II was lost in October 2003. Therefore in this study only AMSR-E data is used.

The main advantage of AMSR-E in comparison to SSM/I is its improved spatial resolution. For the 89 GHz channels used here the resolution is improved by factor three in comparison to SSM/I 85 GHz channels (SSM/I footprint size: 13x15 km², AMSR-E footprint size: 4x6 km²) and the footprint area is reduced from 153 km² to 19 km². The spatial resolution of ice concentration derived using the widespread NASA-Team and Bootstrap sea ice concentration algorithms is restricted to the one of the involved channels with the coarsest resolution, i.e. the 19 GHz channels, that is 43x69 km² for SSM/I and 16x27 km² for AMSR-E. Thus, the sea ice concentrations presented here represent an improvement in linear spatial resolution of more than a factor of three compared to non-89 GHz AMSR-E based sea ice concentration, and an improvement of more than ten times compared to the resolution of the SSM/I-based ice concentration based on the 37 and 19 GHz channels.

2. Data Set

The AMSR-E measures at six different frequencies between 6.9 to 89 GHz at both horizontal and vertical polarization. For details of the AMSR-E characteristics see Table 1. In this study both 89 GHz channels are used to determine

the sea ice concentration. The lower frequencies are only involved as weather filters to detect spurious ice in the open ocean, and for validation purposes. AMSR-E and AMSR were developed by the National Space Development Agency of Japan (NASDA) now renamed to Japan Aerospace Exploration Agency (JAXA). The AMSR-E Level 1A data used is processed by JAXA and then within hours after acquisition distributed by the National Snow and Ice Data Center (NSIDC). From the raw observation counts of the Level 1A data physical brightness temperatures are calculated using the method given in the “AMSR-E Data Users Handbook” [JAXA, 2005]. Most of the following calculations of ice concentration are performed on swath data. Thereafter the ice concentration data are interpolated into the desired geographical grid. All proposed methods work as well with interpolated gridded brightness temperature data, but as the algorithm proposed here is not a linear function of brightness temperature this may lead to slightly different results. However, comparison tests between ASI ice concentrations calculated on swath data and on Level 3 gridded brightness temperatures from NSIDC show mean differences below 1%, which is well within the error margin. In sections 4.1 and 4.2 such Level 3 grid ASI ice concentration are used on the same interpolated grid as the NASA-Team 2 and Bootstrap ice concentration for comparison.

3. ARTIST Sea Ice Algorithm

An extensive field program with ground based and airborne measurements in the area around Svalbard was conducted during the research project ARTIST (Arctic Radiation and Turbulence Interaction Study) in March and April 1998. The ARTIST Sea Ice (ASI) algorithm used here was

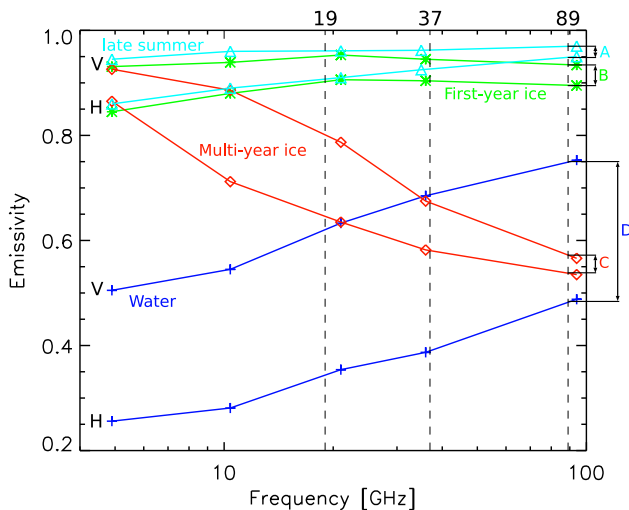


Figure 1. Vertical (V) and horizontal (H) emissivity of sea ice and sea water measured at an incident angle of $\theta = 50^\circ$ for different frequencies. The vertical lines show the intersect with the AMSR-E frequencies at 19, 37, and 89 GHz. In winter *NORSEX Group* [1983] measured first-year (green with stars), multi-year ice (red with diamonds), and sea water (blue with crosses) at 4.9, 10.4, 21, 37, and 94 GHz. In late summer *Onstott et al.* [1987] measured mixed first-year and multi-year ice (cyan with triangles) at 4.9, 10.4, 21, 35, and 94 GHz. At 89 GHz the emissivity differences A, B and C for the different ice types are similar and much smaller than the emissivity difference D of water.

originally developed to benefit from the high spatial resolution of the 85 GHz channels of the SSM/I sensor for the mesoscale numeric modeling of the polar atmospheric boundary layer in the marginal sea ice zone [Kaleschke *et al.*, 2001]. It is an enhancement of the Svendsen sea ice algorithm for frequencies near 90 GHz [Svendsen *et al.*, 1987]. One advantage of the ASI algorithm in contrast to other 85 GHz algorithms [e.g. Kern, 2004] is that it does not need additional data sources as input. It shows a performance similar to other sea ice algorithms [Kern *et al.*, 2003].

The ice concentration is calculated by the value of the polarization difference P of the brightness temperatures T_B ,

$$P = T_{B,V} - T_{B,H} \quad (1)$$

with V for vertical and H for horizontal polarization. It is known from surface measurements that the polarization difference of the emissivity near 90 GHz is similar for all ice types and much smaller than for open water (Figure 1). This is also true for the brightness temperature polarization difference P , as the physical temperature is identical for horizontally and vertically polarized brightness temperatures and thus only emissivity differences influence P . For the influence of the atmosphere a_c on the polarization difference we use

$$P = P_s e^{-\tau} (1.1 e^{-\tau} - 0.11) = P_s a_c \quad (2)$$

with atmospheric opacity τ and surface polarization difference P_s . This approximation is valid for a horizontally stratified atmosphere under Arctic conditions with an effective temperature replacing the vertical temperature profile and a diffusely reflecting surface viewed under an incidence angle of approximately 50° [Svendsen *et al.*, 1987]. Thus the polarization difference in dependence of the ice concentration C can be written as

$$P(C) = \underbrace{(C P_{s,i} + (1 - C) P_{s,w})}_{P_s} a_c \quad (3)$$

where $P_{s,i}$ and $P_{s,w}$ are surface polarization differences for ice and water, respectively. The atmospheric influence a_c in general is a function of the ice concentration [Svendsen *et al.*, 1983, 1987]. With equation (3) the polarization difference P_0 for the ice concentration $C = 0$ (open water) and atmospheric influence a_0 is given by

$$P_0 = a_0 P_{s,w} \quad (4)$$

and similarly for the ice concentration $C = 1$ (closed ice cover) by

$$P_1 = a_1 P_{s,i} \quad (5)$$

Taylor expansions of equation (3) around $C = 0$ and $C = 1$ lead to

$$P = a_0 C (P_{s,i} - P_{s,w}) + P_0 \quad \text{for } C \rightarrow 0 \quad (6)$$

$$P = a_1 (C - 1) (P_{s,i} - P_{s,w}) + P_1 \quad \text{for } C \rightarrow 1 \quad (7)$$

if all higher terms are neglected. Additionally the derivatives of the atmospheric influence a'_0 for $C = 0$ and a'_1 for $C = 1$ are considered to be zero, assuming the variation of the atmospheric influence to be small for totally ice covered or open water areas. With equations (4) and (5) the dependence of the atmospheric influence can be substituted and the ice concentration is given by:

$$C = \left(\frac{P}{P_0} - 1 \right) \left(\frac{P_{s,w}}{P_{s,i} - P_{s,w}} \right) \quad \text{for } C \rightarrow 0 \quad (8)$$

$$C = \frac{P}{P_1} + \left(\frac{P}{P_1} - 1 \right) \left(\frac{P_{s,w}}{P_{s,i} - P_{s,w}} \right) \quad \text{for } C \rightarrow 1. \quad (9)$$

Table 1. AMSR-E Main Characteristics [JAXA, 2005].

Center Frequency [GHz]	6.925	10.65	18.7	23.8	36.5	89	
						A Scan	B Scan
Band Width [MHz]	350	100	200	400	1000	3000	3000
3 dB Beam Width	2.2°	1.5°	0.8°	0.92°	0.42°	0.19°	0.18°
Footprint Size [km ²]	43 × 75	29 × 51	16 × 27	18 × 32	8.2 × 14.4	3.7 × 6.5	3.5 × 5.9
Sampling Interval [km ²]	9 × 10	9 × 10	9 × 10	9 × 10	9 × 10	4.5 × 5	4.5 × 5
Temperature Resolution [K]	0.33	0.54	0.48	0.45	0.45	0.98	1.12
Integration Time [ms]	2.5	2.5	2.5	2.5	2.5	1.2	1.2
Incidence Angle	55°	55°	55°	55°	55°	55°	54.5°
Dynamic Range	2.7–340 K						
Polarization	Vertical and Horizontal						
Cross Polarization	Less than −20 dB						
Swath Width	1450 km nominal						

For Arctic conditions $P_{s,w}/(P_{s,i} - P_{s,w}) = -1.14$ is a typical value for sea ice signatures [Svendsen *et al.*, 1987]. To be able to retrieve all ice concentration values between 0% and 100% we need to interpolate between the solutions of equations (8) and (9). Assuming the atmospheric influence to be a smooth function of the ice concentration C we select a third order polynomial for the sea ice concentration between open water and 100% ice cover:

$$C = d_3P^3 + d_2P^2 + d_1P + d_0. \quad (10)$$

With equations (8) and (9) and their first derivatives the unknowns d_i in equation (10) can be determined by solving the linear equation system:

$$\begin{bmatrix} P_0^3 & P_0^2 & P_0 & 1 \\ P_1^3 & P_1^2 & P_1 & 1 \\ 3P_0^3 & 2P_0^2 & P_0 & 0 \\ 3P_1^3 & 2P_1^2 & P_1 & 0 \end{bmatrix} \begin{bmatrix} d_3 \\ d_2 \\ d_1 \\ d_0 \end{bmatrix} = \begin{bmatrix} 0 \\ 1 \\ -1.14 \\ -0.14 \end{bmatrix}. \quad (11)$$

With thus found d_0 to d_3 , equation (10) can be used to calculate the sea ice concentration if the tie-points P_0 and P_1 for open water and 100% ice coverage are known. C is set equal to zero for $P > P_0$ and equal to one for $P < P_1$.

The correct choice of the tie-points is important for the retrieval of the sea ice concentration as they also include the mean atmospheric influence. For the original Svendsen algorithm it was suggested to choose the maxima and minima of the polarization difference of the according swath as tie points, forming a self-adjusting procedure for different atmospheric conditions [Svendsen *et al.*, 1987]. However, it was found that due to changing atmospheric influence within one swath the maximum (minimum) polarization difference often is not the best representation for open water (100 percent ice cover) and is causing non-physical steps when combining the swaths [Lomax *et al.*, 1995; Kaleschke *et al.*, 2001]. Another study successfully used fixed, hand selected tie points for the Svendsen algorithm during the Arctic Ocean Section expedition between 24. July to 9. September 1994 [Lubin *et al.*, 1997]. This led to the approach of the ASI algorithm: It uses fixed tie-points that are found by comparing ice concentration of the Svendsen algorithm with well validated reference ice concentration from an independent source. The tie-points can for example be obtained from the lower frequency channels of the radiometer which suffer less from the atmospheric influence. Details are discussed in section 4.

3.1. Weather Filters

One disadvantage of the 89 GHz channels is the pronounced influence of atmospheric cloud liquid water and water vapor on the brightness temperatures. Especially cyclones over open water can reduce the polarization difference to values similarly small as those of sea ice. Therefore effective filters are necessary to remove spurious ice concentration in open water areas. The weather filtering process

consists of three steps. All of them use the lower frequency channels with lower spatial resolution. This does not lead to a lower resolution of the marginal ice zone [Kaleschke *et al.*, 2001] but it may cause pixels along the ice edge to show too high ice concentrations due to missing weather filters. If this is the case the resolution of the ice edge is determined by the resolution of the weather filter.

The weather filtering steps are:

a) The first weather filter uses the gradient ratio (GR) of the 36.5 and 18.7 GHz channels [Gloersen and Cavalieri, 1986] which is positive for water but near zero or negative for

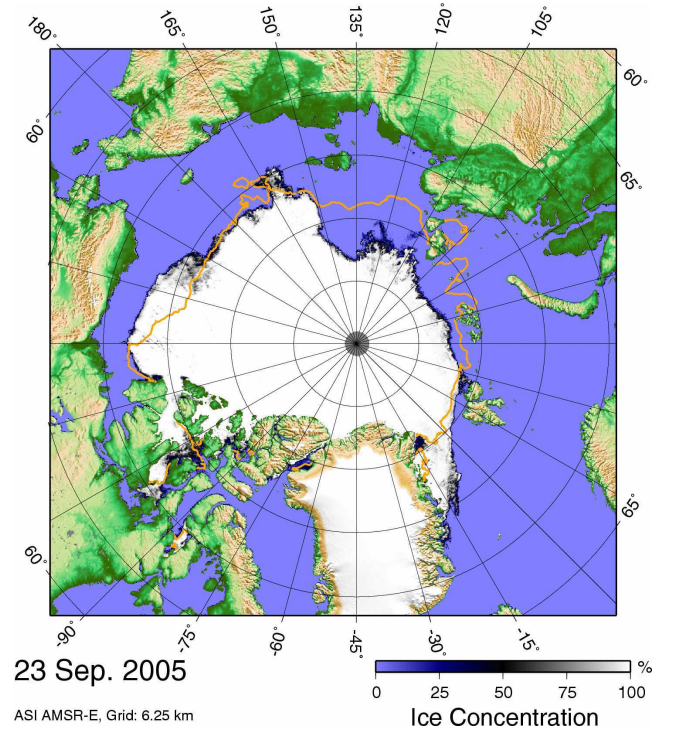


Figure 2. Arctic sea ice concentration map calculated from AMSR-E data using the ASI algorithm (Tie-points $P_0 = 47$ K, $P_1 = 11.7$) showing the minimum ice extent for 2005. Sea ice area and extent showed an absolute minimum in September 2005 since the beginning of satellite sea ice observations in 1972. In orange the 50% contour of the mean September sea ice concentration during the AMSR-E measurement period 2002 to 2005 is shown. In contrast to the scientific color table of Figure 3 a more intuitive color table is used to visualize the ice concentration for non scientific users.

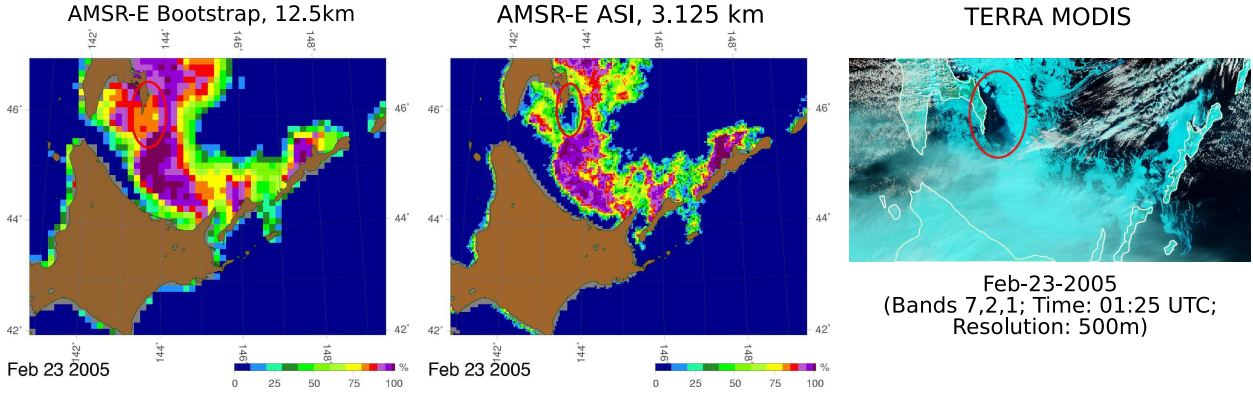


Figure 3. Comparison of ice concentration on 23 February 2005 in the Sea of Okhotsk. The left image shows the Bootstrap ice concentrations in a 12.5 km grid which matches the spatial resolution of the data. The middle image shows the ASI ice concentrations on a 3.125 km grid. The color code gives the ice concentration between 0 and 100%, missing data is marked grey and land is shown in brown. The red ellipse marks a region of open water which is clearly visible in the ASI ice concentrations and the MODIS false color image of that day (right image; bands 7,2,1 (2155 nm, 876 nm, 670 nm); image courtesy of MODIS Rapid Response Project at NASA/GSFC) but is not visible in the Bootstrap data due to the lower resolution.

ice. This ratio mainly filters high cloud liquid water cases:

$$GR(36.5/18.7) = \frac{T_B(36.5, V) - T_B(18.7, V)}{T_B(36.5, V) + T_B(18.7, V)} \quad (12)$$

Fourteen scatter plots $GR(36.5/18.7)$ vs. the 18.7 GHz polarization ratio distributed over all seasons and both hemispheres were analyzed to find an optimal threshold which does not filter out too many low ice concentrations but cuts off all spurious ice [Spreen, 2004]:

$$GR(36.5/18.7) \geq 0.045 \Rightarrow C(ASI) = 0. \quad (13)$$

This threshold at least keeps all ice concentrations above 15% which is in general defined as the ice edge contour line [Gloersen et al., 1992; Cavalieri and St. Germain, 1995].

b) To additionally exclude high water vapor cases above open water the gradient ratio $GR(23.8/18.7)$ is used [Cavalieri et al., 1995]. By again analyzing scatter plots analogue to a) a second threshold was found [Spreen, 2004]:

$$GR(23.8/18.7) \geq 0.04 \Rightarrow C(ASI) = 0. \quad (14)$$

c) Finally all ASI ice concentrations with corresponding Bootstrap ice concentrations equal zero are set to zero:

$$C(Bootstrap) = 0 \Rightarrow C(ASI) = 0. \quad (15)$$

After applying these filters only very few extreme weather events may still cause spurious ice in the open ocean.

An exemplary sea ice concentration map showing the complete Arctic on a 6.25 km polar stereographic grid and using the tie-points $P_0 = 47\text{ K}$ and $P_1 = 11.7\text{ K}$ is shown in Figure 2. On the day shown (23 September), the sea ice extent in the Arctic reached its minimum for 2005. The monthly mean sea ice concentration and extent of the Arctic reached its absolute minimum in 2005 since the beginning of satellite sea ice observations in 1972 [Cavalieri et al., 2003; Comiso, 2002]. For comparison the monthly mean September 50% ice contour of the AMSR-E measurement period 2002 to 2005 is shown in orange. All four years are minimum ice extent years in comparison to the long term mean extent of the past 30 years [Stroeve et al., 2005; Serreze et al., 2003].

An example of the accomplished improvements in the spatial resolution in comparison to more traditional algo-

gorithms using the 19 and 37 GHz channels is demonstrated in a section of the Sea of Okhotsk (Figure 3) where a fraction of open water evolved along the south-easterly end of Sakhalin. A region of open water can be clearly identified in the MODIS (Moderate-Resolution Imaging Spectroradiometer on NASA's Terra satellite) false color image (Figure 3 right) of that day. It is correctly reproduced in the ASI AMSR-E ice concentrations (middle), but not in the Bootstrap AMSR-E ones (left). The coarse resolution of the 18.7 ($\approx 20.1\text{ km}$) and 36.5 GHz ($\approx 10.6\text{ km}$) channels used by the Bootstrap algorithm and all other low frequency algorithms smear out the open water.

4. Validation and Error Estimation

In this section we evaluate the ASI results in comparison to in-situ data and other ice concentration algorithms (Section 4.1), introduce a method to automatically adapt the ASI to reference ice concentrations (Section 4.2), perform a tie-point sensitivity analysis (Section 4.3), and estimate the expected errors by use of in-situ measurements (Section 4.4).

The tie-points P_0 and P_1 are the two modifiable parameters to adjust the algorithm to observations (beside weather filter cut-offs). Most of the validation will therefore focus on their optimal choice. P_0 and P_1 determine the maximum and minimum polarization difference, respectively. All polarization differences above (below) P_0 (P_1) are set to 0% (100%) ice concentration. The atmospheric influence on P_1 is small and all ice types even for different seasons have a similar polarization difference (Figure 1). P_1 therefore has to be the best representation for all ice types in the dataset. The atmospheric influence on P_0 is larger as cloud liquid water and water vapor reduce the polarization difference above water. Additionally the brightness temperatures are influenced by the wind driven roughening of the ocean. Thus the choice of P_0 also includes the general atmospheric influence on the brightness temperatures.

4.1. Constant Tie-points

The time span and region for which a set of tie-points is valid depends on the variability of the atmospheric conditions and the accuracy of the sea ice concentration required for the application at hand.

A 30 days comparison during the Arctic Radiation and Turbulence Interaction Study (ARTIST) of ASI SSM/I

ice concentration with fixed tie-points with those calculated with the NASA-Team algorithm [Cavalieri *et al.*, 1984, 1991, 1995] showed a mean difference of only $(1 \pm 4)\%$ [Kaleschke *et al.*, 2001]. The Arctic Ocean Section expedition between July to September 1994 used the Svendsen SSM/I algorithm with constant tie-points and stated that the ice concentration were at least as good as those obtained by the NASA-Team ice concentration algorithm [Lubin *et al.*, 1997]. However, they stress the enhanced influence of the atmospheric opacity on the 85.5 GHz channels, which may lead to over or underestimation of the sea ice concentration, especially in the marginal ice zone. These findings are also supported by experiences of the Polarstern ARK-XX/2 expedition from July to August 2004 when ASI AMSR-E ice concentration with constant tie-points were processed on board (see Cruise Report ARK XX/2: <http://www.awi-bremerhaven.de/Modelling/SEAICE/icereport04/>). All these studies achieved good results without changing the tie-points.

For our near real time ice maps published in the internet a set of constant tie-points is used through the whole year and for both hemispheres to guarantee consistent ice concentration from day to day. The tie-points $P_0 = 47\text{K}$, $P_1 = 11.7\text{K}$ have been chosen by correlation comparison with AMSR-E Bootstrap ice concentration [Spreen, 2004]. These tie-points lead to the specific version of equation (10):

$$C = 1.64 \cdot 10^{-5} P^3 - 0.0016 P^2 + 0.0192 P + 0.9710 \quad (16)$$

For regional studies adjusted tie-points may yield better results. For example a different set of tie-points was used during Polarstern expedition ARK-XX/2 ($P_0 = 50\text{K}$, $P_1 = 9\text{K}$) which visually better represented the ice concentration around the ship as observed during helicopter surveys. With the operational tie-points $P_0 = 47\text{K}$, $P_1 = 11.7\text{K}$ the ice concentration was slightly overestimated, as can be seen in the next section.

4.1.1. Comparison to Ship Based Observations

During R/V Polarstern cruises ARK-XIX/1 (6 March to 21 April 2003) and the already mentioned cruise ARK-XX/2 (24 July to 18 August 2004) sea ice conditions around the vessel were routinely observed from the bridge by the on board scientist by visual surveillance. The winter/spring cruise ARK-XIX started in the Storfjorden and Barents Sea and continued along the west coast of Spitzbergen up to 82°N in the Fram Strait. The summer cruise ARK-XX started in Longyearbyen and went through the Greenland Sea through Fram Strait up to 85°N . One of the several observed quantities is the total sea ice concentration, which is shown as gray lines in Figure 5 for ARK-XIX (left) and ARK-XX (right), respectively. Details can be found in Lieser [2005], the datasets including photos of every observation are available through Lieser *et al.* [2005] and Lieser and Haas [2005]. As the observation were conducted by up to 16 different persons, errors may be introduced due to different subjective estimates of the ice concentration around the ship. The ice concentration estimates represent the area visible from the vessels bridge. This area depends on the overall visibility (fog, haze etc.) and thus is often considerably smaller than the AMSR-E 89 GHz footprint and certainly smaller than the 36.5 GHz and 18.7 GHz footprints. Still these are valuable in-situ data for validation of sea ice concentration algorithms.

These in-situ observations are compared to three different AMSR-E sea ice concentration data sets: (1) ASI ice concentrations on a 6.25 km grid using the operational tie-points $P_0 = 47\text{K}$ and $P_1 = 11.7\text{K}$, (2) NASA-Team 2 ice concentrations on a 12.5 km grid [Markus and Cavalieri, 2000], which is the standard ice concentration data available from NSIDC [Cavalieri and Comiso, 2004], and (3) ice concentrations from the Basic Bootstrap algorithm [Comiso *et al.*, 1997] on a 12.5 km grid, which are provided as differences to

NASA-Team 2 in the NSIDC data set, too. The differences between these three algorithms and the Polarstern data are shown in Figure 5.

The correlation between Polarstern and ASI is 0.79/0.80, the correlation with NASA-Team 2 amounts to 0.78/0.79, and the correlation with Bootstrap is 0.78/0.83 for ARK-XIX/ARK-XX, respectively. The mean difference between ASI and Polarstern is $-3\% \pm 19\%$, $-1\% \pm 17\%$ between NASA-Team 2 and Polarstern, and $-4\% \pm 17\%$ between Bootstrap and Polarstern for cruise ARK-XIX. For cruise ARK-XX the mean differences are $12\% \pm 15\%$ for ASI minus Polarstern, $11\% \pm 15\%$ for NASA-Team 2 minus Polarstern, and $10\% \pm 14\%$ for Bootstrap minus Polarstern. The \pm values give one standard deviation.

During both Polarstern campaigns all three ice concentration algorithms are performing quite similar. During the winter campaign ARK-XIX all algorithms reproduce the Polarstern ice concentration estimates quite well with a small overall underestimation, which is small compared to the standard deviation and caused by outliers in only short periods, where Polarstern mostly operated in the marginal ice zone and the total ice concentration was low (Figure 5). For low ice concentrations the expected error for all algorithms is larger than for high ice concentrations (see Section 4.4). But here the main reason for the large differences at low ice concentrations can be attributed to the different spatial resolution and time sampling of the Polarstern and AMSR-E ice concentrations. Polarstern ice concentrations are collected hourly while the AMSR-E ice concentrations are calculated from a mean of several satellite overflights of one day and the ice concentration seen from the bridge of Polarstern might not be representative for the complete area of an AMSR-E grid cell. This is supported by the fact that spikes (sudden changes) in the total ice concentration data directly match spikes in all three ice concentration data sets.

During the summer campaign ARK-XX all three algorithms on average overestimated the Polarstern observations between 10 and 12%. The bias is positive for almost the complete time series. This is in agreement with the experience made during the cruise ARK-XX, where different tie-points were used to better represent the visual inspections from the helicopter (see Section 4.1). Polarstern's cruise track is biased to easy navigable ice conditions. During the winter cruise, where the ice concentrations mostly were

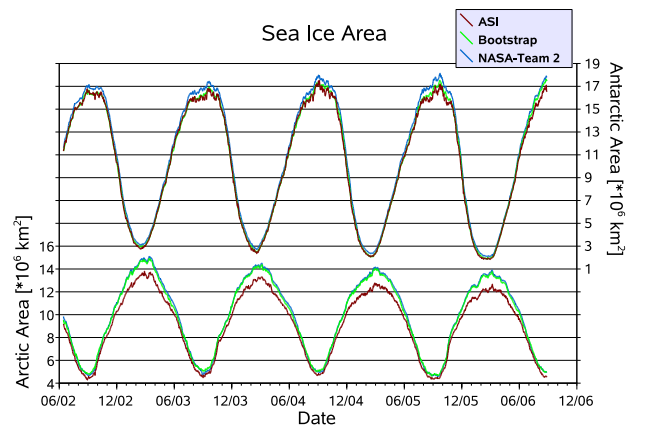


Figure 4. Sea ice covered area in the northern (bottom graphs) and southern (top graphs) hemisphere obtained from AMSR-E data by three different sea ice concentration algorithms: ASI (red), Bootstrap (green), NASA-Team 2 (blue).

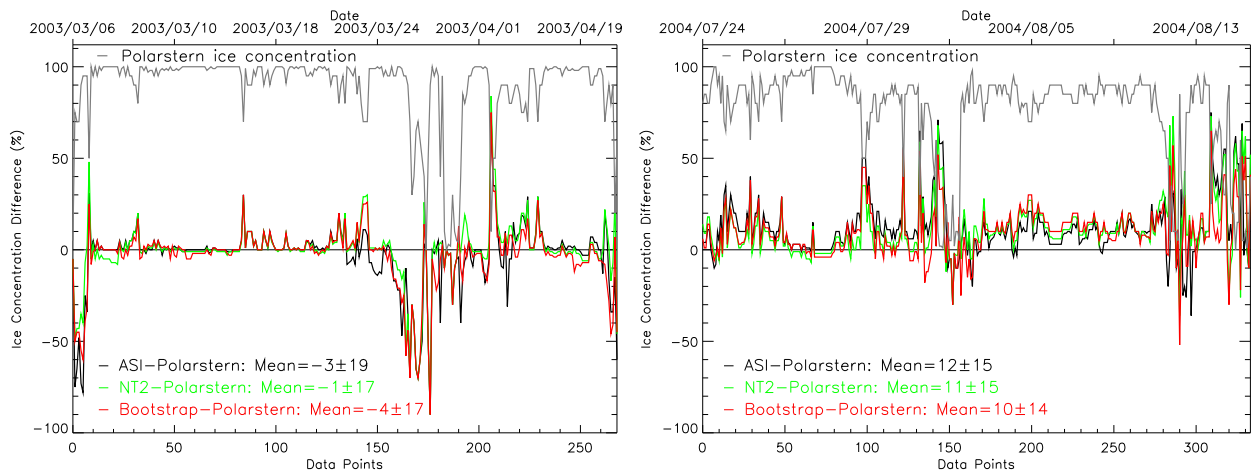


Figure 5. Comparison of three AMSR-E ice concentration algorithm to ship data obtained in the Fram Strait and Greenland Sea region. The absolute sea ice concentration derived by visual inspection from on board the bridge of R/V Polarstern is given as gray graphs. The differences between this in-situ ice concentration and the ASI, NASA-Team 2, and Bootstrap algorithm ice concentration are shown as black, green, and red curves, respectively. The bottom x-axis gives the data point number and the top x-axis the corresponding date. The left graph shows data from expedition ARK-XIX/1 between 6 March and 21 April 2003 and the right graph from expedition ARK-XX/2 between 24 July and 18 August 2004.

near or at 100%, this fact makes not much difference for the ice concentration differences, as the vessel’s captain might prefer leads, but which are mostly refrozen and 100% ice covered. In contrast to the winter cruise, in summer the observed ice concentration seldom exceeds 90%. Now the choice of the vessel’s route through the ice also influences the ice concentration differences, as the ship route might be biased to lower ice concentration compared to the general ice conditions in the AMSR-E footprints. On the other hand, the better representation of the small field of view from the bridge of Polarstern by the higher spatial resolution of the ASI algorithm is not attaining any advantage in comparison to the other two algorithms. This is presumably caused by the enhanced sensitivity of the 89 GHz channels to atmospheric water vapor and cloud liquid water so that the performance of the ASI algorithm is in summer slightly worse than that of the two lower frequency algorithms (Figure 5 right). In winter the performance of ASI is in between that of the Bootstrap and the NASA-Team 2 algorithms (Figure 5 left).

4.1.2. AMSR-E Ice Concentration Algorithm Inter-comparison

To further evaluate the performance of the ASI algorithm in comparison to the Bootstrap and NASA-Team 2 ice concentrations (same data sets as in Section 4.1.1) the complete available AMSR-E time series from 19 June 2002 to 31 August 2006 is considered. Days with large areas of missing data or with spurious ice caused by strong atmospheric influence in at least one of the datasets were discarded. In total 95% of the 1534 days are considered in the Arctic and 96% in the Antarctic. The sea ice area and sea ice extent are often taken as climate change indicators [e.g. Comiso, 2002; Serreze *et al.*, 2003; Stroeve *et al.*, 2005]. Figure 4 shows the sea ice area for the northern (bottom) and southern (top) hemisphere calculated with the three algorithms.

All algorithm show similar results. For the Antarctic small differences occur during winter, where NASA-Team 2 gives the largest results. The amount of the Antarctic winter maxima show a small increase during the AMSR-E measurement period, the four summer minima decrease continuously with 2006 in around $1 \cdot 10^6$ km² less ice area than in 2003. In the Arctic the ASI results are less or equal to those of the Bootstrap and NASA-Team 2 ice area, with higher differences in winter. The ice area is decreasing in

summer and winter for all three algorithms. The decrease of the winter maximum in the four year period is larger than $1.2 \cdot 10^6$ km². The ASI sea ice extent never exceeds the Bootstrap extent because Bootstrap open water areas are used as mask for the ASI data (Section 3.1). For the area differences additionally the different grid resolution has to be considered. Spill over effects along the costs, weather filtering in the marginal ice zone and all other errors which influence a complete grid cell, will affect a larger area for a 12.5 km than for a 6.25 km grid. E.g., the integrated area of polynyas often show differences on the two grid resolutions, as can be seen in the example in Figure 3.

To compare the three data sets with a matched resolution the ASI data are convolved with a Gaussian function with the full width at half maximum set to 21 km, the resolution of the AMSR-E 18.7 GHz channels, and then interpolated on the 12.5 km grid. The spatial distribution of the mean differences during the complete AMSR-E period for ASI minus Bootstrap and ASI minus NASA-Team 2 and the time series of these differences are shown in Figure 6 for both hemispheres.

In the northern hemisphere the mean overall difference for ASI minus Bootstrap is $-1.4\% \pm 8.2\%$ with a mean correlation of 0.95. For ASI minus NASA-Team 2 the mean difference amounts to $-2.0\% \pm 8.8\%$ with a mean correlation of 0.93. In the southern hemisphere ASI minus Bootstrap is on average $1.7\% \pm 10.8\%$ with a correlation of 0.92 and ASI minus NASA-Team 2 is $-1.6\% \pm 7.2\%$ with a correlation of 0.97. The \pm values give again one standard deviation. These results are summarized in Table 2.

The spatial patterns in the maps of both differences show a lot of similarities. In the Arctic the largest differences occur in the dynamic East Greenland Current and along the

Table 2. Mean bias, standard deviations (RMS) and correlation between ASI and Bootstrap, and ASI and NASA-Team 2 sea ice concentrations for the AMSR-E period 19 June 2002 to 31 August 2006.

hemisphere	difference	bias	RMS	correlation
north	ASI – Bootstrap	-1.4	8.2	0.95
	ASI – NASA-Team 2	-2.0	8.8	0.93
south	ASI – Bootstrap	1.7	10.8	0.92
	ASI – NASA-Team 2	-1.6	7.2	0.97

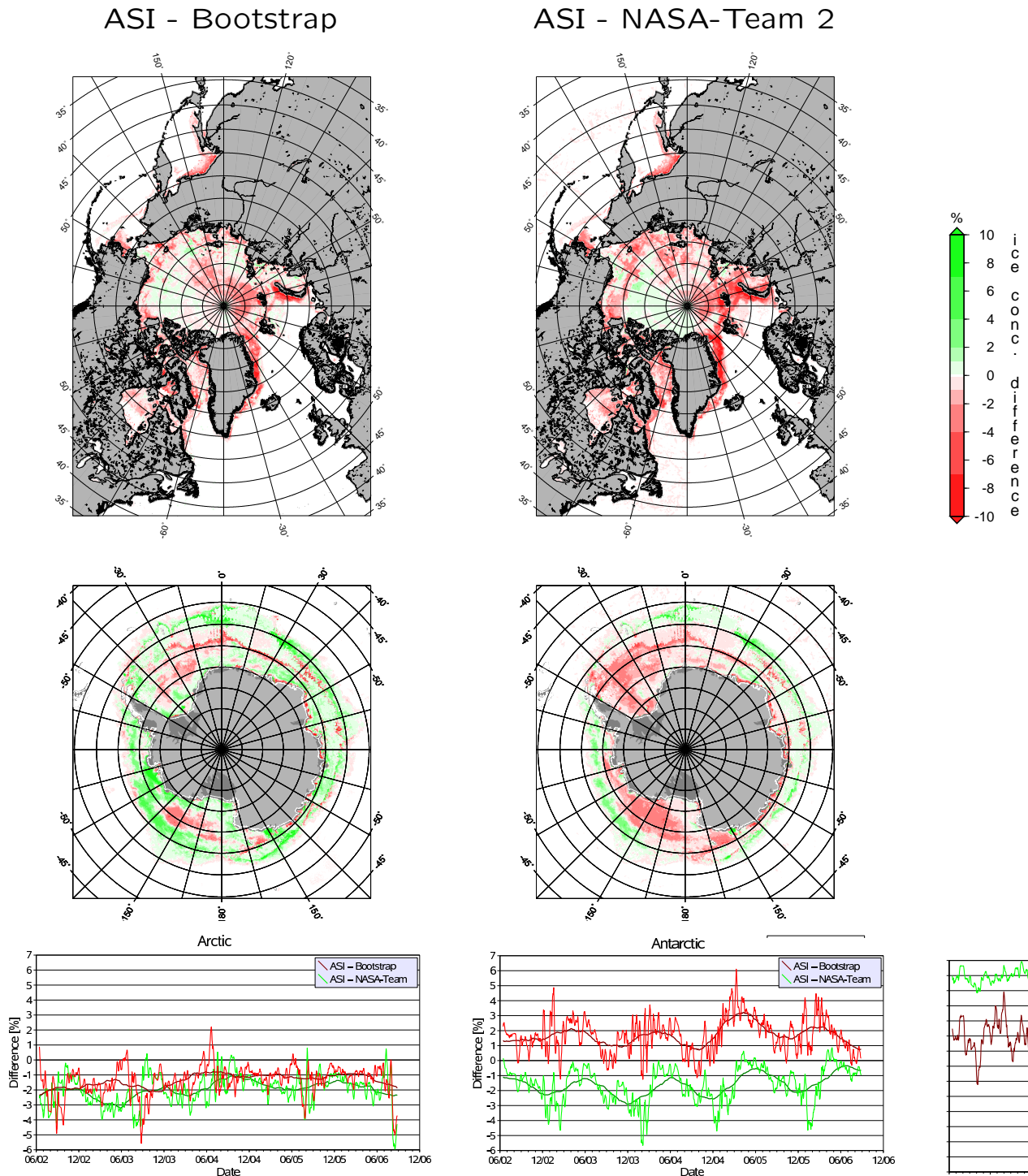


Figure 6. Top and middle row: mean daily difference maps of the period 19 June 2002 to 31 August 2006 of ASI minus Bootstrap (left panels) and ASI minus NASA-Team 2 (right panels) AMSR-E ice concentrations. Top panels show northern hemisphere and middle row panels southern hemisphere results. Bottom row graphs show the time series of the differences for the complete northern hemisphere (left) and southern hemisphere (right). Green curves show ASI minus Bootstrap and red ASI minus NASA-Team 2 results. Bright curves are 7-day and dark 180-day running means. All differences are given in percent ice concentration.

west coast of Novaya Zemlya. In the southern hemisphere the largest differences occur along the coast and there are similar negative differences in both data sets in the Ross Sea (-145° to -180° longitude) and along a zone at -65° latitude starting in the Weddell Sea (30° W) and ranging till 60° W. The latter is an area where the ice edge is rather

stable for some months of each year during the investigation period. Also other locations of stable ice edge can be identified in the differences maps. Thus the ice edge is another region where large differences occur. The absolute value of the mean differences is not exceeding 2% for any of the four cases. This is within the error estimates of all three algo-

rithms (see Sections 4.3, 4.4, and e.g. *Comiso et al.* [1997]). The standard deviations reach 10% but the larger differences mainly occur along the coast and in the marginal ice zone, what will be confirmed in Section 4.4. For three out of the four cases the mean difference is negative and for one it is positive with a similar absolute value. In the Arctic the ASI algorithm seems to slightly underestimate the ice concentration in comparison to the two standard AMSR-E algorithms. In the Antarctic ASI lies well in between the two algorithms.

The bottom graphs in Figure 6 show the time series of the Arctic and Antarctic differences smoothed with a 7-day running mean as bright green (ASI – Bootstrap) and red (ASI – NASA-Team 2) lines and smoothed with a 180-day running mean as darker red and green lines. The 7-day smoothed time series shows high variability with a lot of changes on the scale of few days. As this is the typical time scale of weather systems we suppose that these changes represent the fast changing atmospheric influence. The 180-day smoothed curves show a clear seasonal cycle, which is more pronounced in the Antarctic. We expect that using seasonally changing tie-points as suggested in Section 4.2 the here observed seasonal differences could be reduced. A hemispherical different set of tie-points for Arctic and Antarctic could also reduce the differences. But as we do not know which of the three algorithms is best represents the truth, an adaption based only on differences is questionable. Nevertheless, for applications where not the best representation of the truth but minimal differences between two algorithms is worthwhile, an adaption of the tie-points like the one described in the next section should be used.

4.2. Automatic Adaptation of Tie-points

In order to obtain more insight into seasonal and regional stability of the tie-points, a method to automatically adapt them to reference ice concentrations was developed. Moreover, with this method the ASI ice concentrations can adopt statistical properties like the mean of a spatially lower resolved algorithm. This is useful if two datasets should be merged with the mean kept homogeneous, but the higher spatial resolution of the ASI data is needed. We employed an iterative simplex method to minimize the mean square error (MSE) between ASI AMSR-E and NASA-Team SSM/I ice concentrations. For the four years 2003 to 2006, which are completely covered by AMSR-E data, AMSR-E ASI ice concentrations are compared to SSM/I NASA-Team ice concentrations from NSIDC [*Cavaliere et al.*, 1996, updated 2006; *Meier et al.*, 2006, updated quarterly]. We have selected the SSM/I NASA Team ice concentrations in order to use two data sets which are as independent as possible. They are completely independent with respect to the influence of the sensor. However, even though both algorithms use different frequency channels, they are not independent with respect to geophysical noise (atmospheric influence) and both algorithms use polarization information.

The method of *Nelder and Mead* [1965] performs multi-dimensional minimization of a function. Here the two free variables P_0 and P_1 of the ASI algorithm are used to minimize the MSE. The *Nelder and Mead* [1965] algorithm does not contain any constraints for the geophysically significance of the found solution. To keep some constraint for the open water tie-point P_0 of the ASI in the automatic adaption procedure, we did not apply the Bootstrap ice concentrations as third weather filter (see paragraph c) in Section 3.1). This keeps some small open water area not set to zero by the weather filters and the ASI algorithm has to take care of those by itself. Otherwise the solution of the minimization might contain unphysically large polarization differences for P_0 , if this solution minimizes the MSE for the ice covered

regions. With some water areas kept unfiltered, large values for P_0 would cause spurious ice to appear in the open water areas, which would increase the MSE. By this method P_0 is kept in a physical codomain.

To compare data with the same resolution the ASI AMSR-E ice concentration grids are convolved with a Gaussian distribution with the full width at half maximum set to the resolution of the SSM/I 19 GHz channels. The MSE

$$S = \frac{1}{n} \sum_{i=1}^n (C_{ASI} - C_{NT})^2 \stackrel{!}{=} \min \quad (17)$$

between these blurred ASI C_{ASI} and the NASA-TEAM ice concentrations C_{NT} is minimized using the *Nelder and Mead* [1965] numerical iterative convergence method. The number of data points is given by n . The method is robust for overdetermined equation systems and for meaningful chosen starting points (we used $P_1 = 8$ K and $P_0 = 50$ K) the algorithm converges.

The tie-point adaptation was carried out for the four years 2003 to 2006 (Arctic: 1449 days, Antarctic: 1450 days, remaining days had data errors) over the complete Arctic and Antarctic regions defined by the grid given in *NSIDC* [1996]. The monthly means with standard deviation of the thereby found tie-points together with the 30-day running mean curves of the four individual years are shown in Figure 7.

The mean MSE of all four years results in 0.013 ± 0.006 for the Arctic and 0.014 ± 0.005 for the Antarctic (for ice concentrations scaled between 0 and 1, \pm values give one standard deviation). The resulting mean ice concentration differences between the two data sets are $0.7\% \pm 0.3\%$ and $0.3\% \pm 0.4\%$, respectively, and thus are small. But the mean of the root mean square error (RMSE) between ASI and NASA-Team ice concentration is $\sqrt{S} = 11\% \pm 8\%$ for the

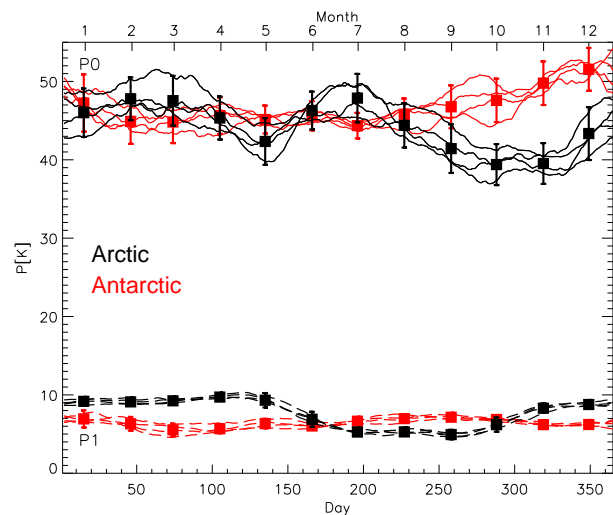


Figure 7. Annual development of AMSR-E ASI tie-points P_0 for open water (top solid curves) and P_1 for ice (bottom dashed curves) found by minimizing the difference to NASA-Team SSM/I ice concentration for the four years 2003 to 2006. Arctic tie-points are shown in black, Antarctic in red color. Squares indicate the four year monthly means of adapted tie-points with bars indicating plus-minus one standard deviation. The curves show the 30-day running mean development of the tie-points of the four individual years 2003 to 2006. Bottom x-axis gives day of year, top x-axis month of year.

Arctic and $\sqrt{S} = 12\% \pm 7\%$ for the Antarctic. Therefore regional difference between the two ice concentration datasets of approximately 10% regularly still occur after the adaptation both in the Arctic and the Antarctic.

The total mean of the derived tie-points shown in Figure 7 is $P_0 = (44 \pm 4)\text{K}$ and $P_1 = (7.7 \pm 1.9)\text{K}$ for the Arctic and $P_0 = (47 \pm 3)\text{K}$ and $P_1 = (6.4 \pm 0.8)\text{K}$ for the Antarctic. The mean polarization difference of all open water areas is $P_{water} = (43 \pm 6)\text{K}$ and $P_{water} = (43 \pm 2)\text{K}$ for the Arctic and Antarctic, respectively, which agrees well with P_0 tie-points found by the adaptation scheme.

The tie-points show a seasonal cycle, which amplitude is both for P_0 and P_1 larger in the Arctic than in the Antarctic. The seasonal cycle of P_1 for all four years is very similar, both in the Arctic and Antarctic. In summer (Arctic: Jun to Oct, Antarctic: Dec to Apr) P_1 in the Arctic is smaller ($P_1 = 5.7\text{K}$) than during the winter period ($P_1 = 9.1\text{K}$), while for the Antarctic the summer to winter difference is present but smaller than 1 K.

The developing of the open water tie-point P_0 is also very similar for all four years, but no clear summer to winter discrimination can be made. The smallest P_0 values occur to the end of summer (Arctic: Oct-Nov, Antarctic: Feb-Mar), when the ice extent is at its minimum. The highest P_0 values occur to the beginning of summer in July and December for Arctic and Antarctic, respectively. To the end of summer higher wind speeds might reduce the polarization difference of open water, which could lead to a smaller P_0 tie-point, as the tendency for ice misclassification in the open water areas is intensified for larger P_0 's.

All these differences are due to the enhanced atmospheric influence on the brightness temperature during the summer months and the change in radiometric properties of the ice caused by melting and refreezing. Therefore it might be useful for some studies to use seasonal, monthly or even daily adapted tie-points. Note that the tie-point adaptation is performed to another ice concentration algorithm and not to ground truth data. The changes of the tie-points during the year therefore can also be attributed to changes between the brightness temperatures at the different frequencies used by the two algorithms. E.g. the lower frequencies might be stronger affected by snow and ice layering which due to the adaptation will then show up in the higher frequency algorithm, too.

This tie-point adapting scheme can easily be implemented operationally and fully automatic, if reference ice concentrations are available on the same time bases. It can for example be used to obtain ice concentration from two different data sets and algorithms but with best possible accordance. E.g. the adapted tie-point presented here can be used to smoothly extend the SSM/I NASA-Team time series with AMSR-E ASI data offering a higher spatial resolution.

A daily regional adaptation of the tie-points to ice concentration obtained from lower frequency channels than 89 GHz or totally independent obtained ice concentration has the advantage of reducing the overall atmospheric influence on the ice concentration in the study area, as the ASI ice concentration are then always drawn towards the atmospherically less influenced ice concentration. Nevertheless, the atmospheric influence of small scale or mesoscale cyclones which cause strong horizontal gradients of the atmospheric influence (total water vapor and liquid water path) within the study area may not be completely compensated.

For two reasons we keep using the fixed tie-points presented in section 4.1 for our operational ice maps:

1. The reference ice concentration are taken as truth, and their potential errors will propagate into the ASI ice concentration on top of the differences of up to 10% between reference and adapted ASI ice concentration as shown above. Employing the annual mean adapted tie points derived above using the NASA-Team ice concentration as reference may lead to an underestimation of the ice concentration by the ASI algorithm with respect to other reference data like optical MODIS images. The NASA-Team algorithm is known to represent the lower limit of the effective ice concentration [e.g. *Comiso et al., 1997*]. With the

adapted tie-points the ASI ice concentration are up to 10% different and therefore in some cases even 10% lower than the NASA-Team ice concentration.

2. Changing the tie-points seasonally or even monthly and daily may cause discontinuities in the time series of the ice concentration at each time of change which is unfavorable for long-term studies.

For these reasons fixed tie-points are used for the hemispheric and long-term data products. In future a smooth function for the changing tie-points might be used. However, for regional studies where reliable reference ice concentrations are available even just for short time periods or for just a spatial subset of the study area (e.g. SAR data) adapted tie-points may yield better results than fixed ones.

4.3. Tie-point Sensitivity Analysis

The tie-points P_0 and P_1 may vary first with each overflight due to changing atmospheric influence (equations (4) and (5)), second on the scale of weeks due to changing radiative properties of the surfaces caused by atmospheric influence (temperature, rain and snow) [e.g. *Voss et al., 2003*] and third with the seasons (Figure 7). Moreover, when using the method of section 4.2, the tie-points depend on the used calibration data set. E.g. the fixed tie-points of section 4.1 found by comparison with AMSR-E Bootstrap ice concentration differ from the adaptive tie-points in section 4.2. For all these reasons there will always be a difference between the true and the used tie-points.

To estimate the influence of small errors in the tie-points on the sea ice concentration results, a sensitivity analysis has been carried out. The constant tie-points $P_0 = 47\text{K}$ and $P_1 = 11.7\text{K}$ of section 4.1 which are also used in the operational analyzes were chosen as reference. The sea ice concentration C in equation (10) is a function of the polarization difference P and the tie-points P_0 and P_1 , as they are needed to determine the coefficients d_i in equation (10): $C = C(P, P_0, P_1)$. These three variables P , P_0 and P_1 were varied separately between -4 and 4K from their reference values. Then the value of the difference ΔC between the varied and the reference ice concentration was calculated. For example for P_0 this leads to

$$\Delta C = C(P, P_0, P_1) - C(P, P_0 + w, P_1). \quad (18)$$

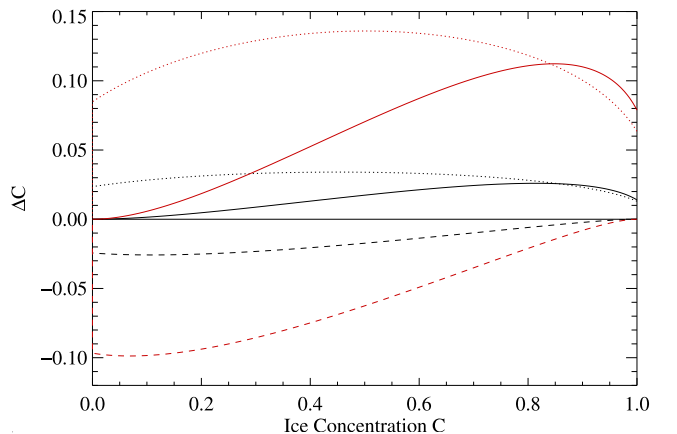


Figure 8. Plot of sea ice concentration differences ΔC between original ice concentration (tie-points $P_0 = 47\text{K}$ and $P_1 = 11.7\text{K}$) and ice concentration where the tie-points were altered by 1 K (black curves) and 4 K (red curves). Dashed: differences for variation of the open water tie-point P_0 by 1 K and 4 K; solid: variation of the ice tie-point P_1 by -1K and -4K ; dotted: variation of P by 1 K and 4 K, respectively.

This leads to the two dashed curves in Figure 8 for $w = 1$ K (black) and 4 K (red), respectively. For P_1 and P , ΔC is calculated accordingly. Additionally P_0 and P_1 were varied simultaneously by $w = [-4 \dots 4]$. Some example results are shown in Figure 8 where ΔC for $w = 1$ K and $w = 4$ K is plotted against the reference ice concentration C . In all these analyzes the difference ΔC never exceeds $\pm 15\%$ and varies linearly in w . The error of P is given by the radiometric resolution of approximately 1 K of the sensor (Table 1), the deviation of P_0 and P_1 from the true value is unknown. However, the seasonal variation of the tie-points in section 4.2 (Figure 7) indicate that the error in P_1 is of the order of 2 K, leading to an error in C of about 6% at ice concentration near 100%. But for P_0 the deviation may exceed even 4 K and the error near 0% ice concentration therefore may be larger than 15%, respectively. These results will be confirmed in the next section.

4.4. Error Estimation

The tie-points P_0 , P_1 depend on the near-surface polarizations $P_{s,w}$ and $P_{s,i}$, respectively, and on the atmospheric opacity τ (equations (2), (3)). In order to estimate the errors introduced into the ASI results by these quantities, results from the ship campaigns NORSEX and MIZEX [Svendsen *et al.*, 1987], when all required quantities were measured simultaneously, are used:

$$\begin{aligned} P_{s,w} &= (82 \pm 4) \text{ K} & P_{s,i} &= (10 \pm 4) \text{ K} \\ \tau_w &= 0.27 \pm 0.1 & \tau_i &= 0.14 \pm 0.035. \end{aligned}$$

The optimal tie-points under these circumstances are found as $P_0 = 46$ K and $P_1 = 7.4$ K by using equation (2). They are kept constant and the standard deviation of the ice concentration σ_C in dependence of C is calculated from equation (3) assuming τ to decrease linearly between τ_w and τ_i . The standard deviation of P is given as:

$$\begin{aligned} \sigma_P &= \sqrt{\left(\frac{\partial P}{\partial \tau}\right)^2 \sigma_\tau^2 + \left(\frac{\partial P}{\partial P_{s,w}}\right)^2 \sigma_{P_{s,w}}^2 + \left(\frac{\partial P}{\partial P_{s,i}}\right)^2 \sigma_{P_{s,i}}^2} \\ &= \left[\begin{aligned} &(C P_{s,i} + (1 - C) P_{s,w})^2 \\ &(-2.2 e^{-2\tau} + 0.11 e^{-\tau})^2 \sigma_\tau^2 \end{aligned} \right] \end{aligned}$$

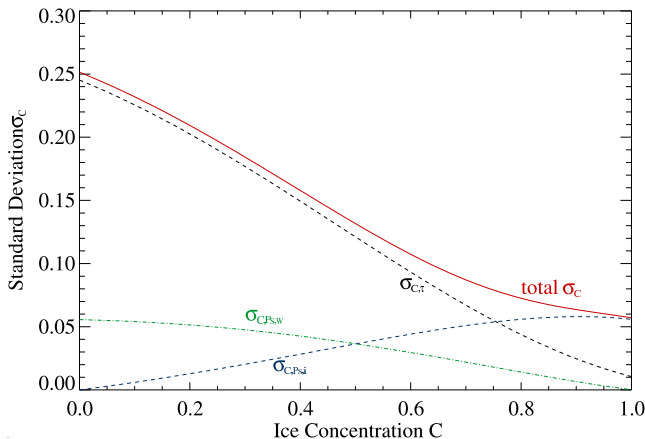


Figure 9. The expected standard deviation σ_C of the ASI ice concentration C using fixed tie-points and standard deviations of τ and P_s obtained during field measurements. The red curve shows the total expected standard deviation of C ; the other, not solid curves show the error contributions of the atmosphere (black short dashes, $\sigma_{C,\tau}$), and of the surface polarization differences of open water (green dash-dotted, $\sigma_{C,P_{s,w}}$) and sea ice (blue long dashes, $\sigma_{C,P_{s,i}}$).

$$\begin{aligned} &+ \left(e^{-\tau} (1.1 e^{-\tau} - 0.11) (1 - C) \right)^2 \sigma_{P_{s,w}}^2 \\ &+ \left(e^{-\tau} (1.1 e^{-\tau} - 0.11) C \right)^2 \sigma_{P_{s,i}}^2 \end{aligned} \Bigg]^{1/2}. \quad (19)$$

With equation (10) follows for the standard deviation of C :

$$\sigma_C = \left| \frac{\partial C}{\partial P} \sigma_P \right| = \left| (3d_3 P^2 + 2d_2 P + d_1) \sigma_P \right|. \quad (20)$$

As seen in Figure 9, σ_C decreases from 25% for $C = 0\%$ to 5.7% for $C = 100\%$. Above $C = 65\%$, σ_C is smaller than 10%. This gives an impression about the error introduced through day by day and regional variations of the atmospheric opacity and the surface polarization difference if reliable tie-points are used.

Another error is introduced by the measuring accuracy of the AMSR-E radiometer of about 1 K at 89 GHz (see Temperature Resolution in Table 1). Additional calculations show that its influence on the ASI ice concentration is below 3.7% [Spreen, 2004].

The assumed accuracy of the lower frequency algorithms is approximately 7%, but also cases with discrepancies up to 30% have been observed [Comiso *et al.*, 1997]. For high ice concentration values the ASI algorithm fits well into this range. For low ice concentration the algorithm may significantly overestimate in cases of high cloud liquid water content, especially when cyclones cross the ice edge. On the other hand the 89 GHz channels are less affected by ice types, refrozen meltponds and snow layering, however they are sensitive to the density and grain size of the snow on top of the sea ice [Tonboe *et al.*, 2005].

5. Discussion and Conclusions

Today the 89 GHz channels of AMSR-E offer the highest spatial resolution for extraction of daily available, global sea ice concentration data. The ASI ice concentration algorithm uses an empirical model to retrieve the ice concentration between 0% and 100%. It also includes a statistical model about the atmospheric influence. Even if the set of tie-points is not adapted daily to the changing atmospheric and surface conditions, the algorithm shows appropriate results especially at mid and high ice concentrations (above 65%), where the error should not exceed 10%. In areas with low ice concentration depending on the atmospheric conditions substantial deviations may occur. In general our comparisons show that the ASI algorithm is performing with a similar quality than two other AMSR-E sea ice algorithms. The enhanced atmospheric influence is not causing a significant different sea ice distribution.

This finding is supported by a recent study comparing seven of the most frequently used SSM/I sea ice concentration algorithms [Andersen *et al.*, 2006]. Over high concentration sea ice it was found that those with the shorter penetration depth, i.e., using mainly near-90 GHz information, tend to produce significantly better statistics than the algorithms at 19 and 37 GHz that are most frequently used nowadays. It was found that during winter the root mean square difference of the near-90 GHz ice concentrations with respect to the ship and SAR data used as reference was consistently smaller. Andersen *et al.* [2006] also investigated the influence of using different ice concentration algorithms on the linear trends in time series of Arctic sea ice area and extent for the period 1991 to 2005. The differences in trends were significant between 15 and 20 % of the total downgoing trend in winter. The differences in winter trends are caused by systematic changes of both the atmospheric and sea ice surface properties in the Arctic during this period. Together with the results of this study it can be stated that

some shortcoming near 90 GHz of stronger atmospheric influence is compensated by less sensibility to surface effects (e.g. snow layering).

As experience shows, for practical navigation purposes ice maps with more than three times higher spatial resolution compared to conventional passive microwave ice maps are preferred, even at the expense of a reduced accuracy in ice concentration for cases with large atmospheric influence. Hemispherical (6.25 km grid) and regional (3.125 km grid) sea ice concentration maps using the ASI algorithm are operationally published by the Institute of Environmental Physics, University Bremen (www.iup.physik.uni-bremen.de) on a daily basis using the data of the day before. All maps are available with two different color tables. A more intuitive blue/white color table like in Figure 2, and the one of Figure 3, which allows to distinguish quantitatively the ice concentration in steps of 1 to 10%.

Systematic sea ice concentration uncertainties affect climate model variables (e.g. the surface air temperature) nearly linearly [Parkinson et al., 2001]. However, regional atmospheric models will benefit of the increased horizontal resolution of the ice concentration data presented in this study, as open water areas and thus the heat transfer is better resolved, see Kaleschke et al. [2001] for an example based on SSM/I data.

Additionally the increased resolution reduces the errors due to mixed coastal pixels. This is particularly useful when mapping coastal polynyas and smaller seas such as the Baltic Sea, Caspian Sea and the Sea of Okhotsk. The polynya area and thus the ocean-atmosphere heat transfer can be estimated with higher accuracy. This is already used for coastal polynyas studies in the Southern Ocean, especially focussing on the dynamics of polynyas [Kern et al., 2006]. Polynya areas derived by the Polynya Signature Simulation Method [Markus and Burns, 1995] using SSM/I data and from ASI AMSR-E ice concentration show good agreement.

As a perspective for future developments, we suggest algorithms with comprehensive modeling of surface and atmosphere, and with the inclusion of prognostic information from numerical weather models. Furthermore, the potential of data assimilation may be of great value.

Acknowledgments. The authors gratefully acknowledge the support of this work under DFG grants He 1746-10/1,2 and SFB 512, and the provision of AMSR-E data by the National Snow and Ice Data center (NSIDC), Boulder, CO, USA and the JAXA EORC (Earth Observation Research and application Center), Tokyo, Japan. The ARTIST project was funded by the Commission of the European Community under Contract No. ENV4-CT97-0497-0487. The code of the Bootstrap algorithm has been kindly provided by J. C. Comiso, NASA Goddard Space Flight Center. We thank the sea ice groups on R/V Polarstern cruises ARK-XIX/1 and ARK-XX/2 for their almost 24 hour observations of sea ice conditions. The reviewers and editors are thanked for their careful and helpful comments, which clearly helped to improve the paper.

References

Aagaard, K., and E. C. Carmack (1989), The role of sea ice and other fresh water in the arctic circulation, *J. Geophys. Res.*, *94*(C10), 14,485–14,498.

Andersen, S., R. Tonboe, L. Kaleschke, G. Heygster, and L. T. Pedersen (2006), Intercomparison of passive microwave sea ice concentration retrievals over the high concentration arctic sea ice, *submitted to J. Geophys. Res.*

Cavalieri, D., and J. Comiso (2004), AMSR-E/Aqua daily L3 12.5 km Tb, sea ice conc., & snow depth polar grids, *digital media V001*, National Snow and Ice Data Center, Boulder, CO, USA, 2004, updated daily.

Cavalieri, D. J., and K. M. St. Germain (1995), Arctic sea ice research with satellite passive microwave radiometers, *IEEE GRS-S Newsletter*, *97*(1), 6–12.

Cavalieri, D. J., P. Gloersen, and W. J. Campbell (1984), Determination of sea ice parameters with the NIMBUS-7 SMMR, *J. Geophys. Res.*, *89*(ND4), 5355–5369.

Cavalieri, D. J., J. P. Crawford, M. R. Drinkwater, D. T. Eppler, L. D. Farmer, R. R. Jentz, and C. C. Wackerman (1991), Aircraft active and passive microwave validation of the sea ice concentration from the Defense Meteorological Satellite Program Special Sensor Microwave Imager, *J. Geophys. Res.*, *96*(C12), 21,998–22,008.

Cavalieri, D. J., K. M. St. Germain, and C. T. Swift (1995), Reduction of weather effects in the calculation of sea-ice concentration with DMSP SSM/I, *J. Glaciology*, *41*(139), 455–464.

Cavalieri, D. J., C. L. Parkinson, P. Gloersen, and H. J. Zwally (1996, updated 2006), Sea ice concentrations from Nimbus-7 SMMR and DMSP SSM/I passive microwave data, [years 2003 to 2005], Boulder, Colorado USA: National Snow and Ice Data Center. Digital media.

Cavalieri, D. J., C. L. Parkinson, and K. Y. Vinnikov (2003), 30-year satellite record reveals contrasting arctic and antarctic decadal sea ice variability, *Geophys. Res. Lett.*, *30*(18), 1970, doi:10.1029/2003GL018031.

Comiso, J. C. (2002), A rapidly declining perennial sea ice cover in the Arctic, *Geophys. Res. Lett.*, *29*(20), 1956, doi: 10.1029/2002GL015650.

Comiso, J. C. (2003), Large-scale characteristics and variability of the global sea ice cover, in *Sea Ice, An Introduction to its Physics, Chemistry, Biology, and Geology*, edited by D. Thomas and G. S. Dieckman, pp. 112–140, Blackwell Publishing, Malden, USA.

Comiso, J. C., D. J. Cavalieri, C. L. Parkinson, and P. Gloersen (1997), Passive microwave algorithms for sea ice concentration: A comparison of two techniques, *Rem. Sens. Environ.*, *60*(3), 357–384.

Gloersen, P., and D. J. Cavalieri (1986), Reduction of weather effects in the calculation of sea ice concentration from microwave radiances, *J. Geophys. Res.*, *91*(C3), 3913–3919.

Gloersen, P., W. Campbell, D. Cavalieri, J. Comiso, C. Parkinson, and H. Zwally (1992), *Arctic and Antarctic sea ice, 1978–1987: satellite passive-microwave observations and analysis, Scientific and technical information program*, vol. NASA SP-511, National Aeronautics and Space Administration (NASA), Washington, D.C.

JAXA (2005), *AMSR-E Data Users Handbook*, Japan Aerospace Exploration Agency (JAXA), 1401 Numanoue, Ohashi, Hatoyama-machi, Hiki-gun, Saitama, Japan, 350-0302, 3. ed.

Kaleschke, L., C. Lüpkes, T. Vihma, J. Haarpaintner, A. Bochart, J. Hartmann, and G. Heygster (2001), SSM/I sea ice remote sensing for mesoscale ocean-atmosphere interaction analysis, *Can. J. Rem. Sens.*, *27*(5), 526–537.

Kern, S. (2004), A new method for medium-resolution sea ice analysis using weather-influence corrected Special Sensor Microwave/Imager 85 GHz data, *Int. J. Rem. Sens.*, *25*(21), 4555–4582, doi:10.1080/01431160410001698898.

Kern, S., L. Kaleschke, and D. A. Clausi (2003), A comparison of two 85 GHz SSM/I ice concentration algorithms with AVHRR and ERS-2 SAR imagery, *IEEE Trans. Geosci. Rem. Sens.*, *41*(10), 2294–2306.

Kern, S., G. Spreen, L. Kaleschke, S. de la Rosa Höhn, and G. Heygster (2007), Polynya Signature Simulation Method polynya area in comparison to AMSR-E 89 GHz sea-ice concentrations in the Ross Sea and off Adelie Coast, Antarctica, for 2002–2005: First results, *Ann. Glaciol.*, *46*, in press.

Lieser, J. L. (2005), *Sea ice conditions in the northern North Atlantic in 2003 and 2004 Observations during RV POLARSTERN cruises ARKTIS XIX/1a and b and ARKTIS XX/2, Reports on Polar and Marine Research*, vol. 504, 197 pp., Alfred Wegener Institute for Polar and Marine Research, Bremerhaven.

Lieser, J. L., and C. Haas (2005), Sea ice conditions in the Fram Strait during Polarstern cruise ARK-XX/2 (AIROTICA), PANGAEA, online, doi:10.1594/PANGAEA.327055.

Lieser, J. L., C. Haas, and S. Kern (2005), Sea ice conditions in the Svalbard region during POLARSTERN cruise ARK-XIX/1 (CryoVex 2003), PANGAEA, online, doi:10.1594/PANGAEA.272527.

Liu, J., J. A. Curry, and D. G. Martinson (2004), Interpretation of recent Antarctic sea ice variability, *Geophys. Res. Lett.*, *31*(2), Art. No. L02,205, doi:10.1029/2003GL018732.

- Lomax, A. S., D. Lubin, and R. Whritner (1995), The potential of interpreting total and multiyear-ice concentration in SSM/I 85.5 GHz imagery, *Rem. Sens. Environ.*, *54*(1), 13–26.
- Lubin, D., C. Garrity, R. Ramseier, and R. Whritner (1997), Total sea ice concentration retrieval from the SSM/I 85.5 GHz channels during the Arctic summer, *Rem. Sens. Environ.*, *62*(1), 63–76.
- Markus, T., and B. A. Burns (1995), A method to estimate subpixel-scale coastal polynyas with satellite microwave data, *J. Geophys. Res.*, *100*(C3), 4473–4487.
- Markus, T., and D. J. Cavalieri (2000), An enhancement of the NASA team sea ice algorithm, *IEEE Trans. Geosci. Rem. Sens.*, *38*(3), 1387–1398.
- Meier, W., F. Fetterer, K. Knowles, M. Savoie, and M. J. Brodzik (2006, updated quarterly), Sea ice concentrations from Nimbus-7 SMMR and DMSP SSM/I passive microwave data, [year 2006], Boulder, Colorado USA: National Snow and Ice Data Center, Digital media.
- Nelder, J. A., and R. Mead (1965), A simplex method for function minimization, *Computer Journal*, *7*(4), 308–313.
- NORSEX Group (1983), Norwegian remote sensing experiment in a marginal ice zone, *Science*, *220*(4599), 781–787.
- NSIDC (1996), DMSP SSM/I brightness temperature and sea ice concentration grids for the polar regions: User's guide – revised edition, *Tech. rep.*, NSIDC Distributed Active Archive Center, University of Colorado, Boulder, Colorado.
- Onstott, R. G., T. C. Grenfell, C. Mätzler, C. A. Luther, and E. A. Svendsen (1987), Evolution of microwave sea ice signatures during early summer and midsummer in the marginal ice zone, *J. Geophys. Res.*, *92*(C7), 6825–6835.
- Parkinson, C. L., D. Rind, R. J. Healy, and D. G. Martinson (2001), The impact of sea ice concentration accuracies on climate model simulations with the GISS GCM, *J. Climate*, *14*(12), 2606–2623.
- Serreze, M., et al. (2003), A record minimum arctic sea ice extent and area in 2002, *Geophys. Res. Lett.*, *30*(3), 1110, doi:10.1029/2002GL016406.
- Spreen, G. (2004), Meereisfernerkundung mit dem satellitengestützten Mikrowellenradiometer AMSR(-E) – Bestimmung der Eiskonzentration und Eiskante unter Verwendung der 89 GHz-Kanäle, Diplomarbeit (master's thesis), University of Hamburg, prepared at the University of Bremen, Dept. of Physics and Electrical Engineering.
- Stroeve, J. C., M. C. Serreze, F. Fetterer, T. Arbetter, W. Meier, J. Maslanik, and K. Knowles (2005), Tracking the arctic's shrinking ice cover: Another extreme september minimum in 2004, *Geophys. Res. Lett.*, *32*(4), Art. No. L04,501, doi:10.1029/2004GL021810.
- Svendsen, E., K. Kloster, B. Farrelly, O. M. Johannessen, J. A. Johannessen, W. J. Campbell, P. Gloersen, D. Cavalieri, and C. Mätzler (1983), Norwegian remote sensing experiment: evaluation of the NIMBUS 7 Scanning Multichannel Microwave Radiometer for sea ice research., *J. Geophys. Res.*, *88*(NC5), 2781–2791.
- Svendsen, E., C. Mätzler, and T. C. Grenfell (1987), A model for retrieving total sea ice concentration from a spaceborne dual-polarized passive microwave instrument operating near 90 GHz, *Int. J. Rem. Sens.*, *8*(10), 1479–1487.
- Tonboe, R., S. Andersen, L. Toudal, and G. Heygster (2006), Sea ice emission modelling, in *Thermal Microwave Radiation - Applications for Remote Sensing, IET Electromag. Wave Ser.*, vol 52, edited by C. Mätzler, pp. 382–400, IET, London, UK.
- Vavrus, S., and S. P. Harrison (2003), The impact of sea-ice dynamics on the Arctic climate system, *Climate Dyn.*, *20*(7–8), 741–757, doi:10.1007/s00382-003-0309-5.
- Voss, S., G. Heygster, and R. Ezraty (2003), Improving sea ice type discrimination by the simultaneous use of SSM/I and scatterometer data, *Polar Research*, *22*(1), 35–42.
- Wadhams, P. (2000), *Ice in the Ocean*, Gordon and Breach Science Publisher, London.

G. Spreen, Institute of Oceanography, Centre for Marine and Atmospheric Sciences (ZMAW), University of Hamburg, Bundesstr. 53, 20146 Hamburg, Germany. (gunnar.spreen@zmaw.de)

L. Kaleschke, Institute of Oceanography, Centre for Marine and Atmospheric Sciences (ZMAW), University of Hamburg, Bundesstr. 53, 20146 Hamburg, Germany. (lars.kaleschke@zmaw.de)

G. Heygster, Institute of Environmental Physics, University of Bremen, P.O. Box 330440, 28334 Bremen, Germany. (heygster@uni-bremen.de)